Hindawi Publishing Corporation
Advances in Optical Technologies
Volume 2012, Article ID 720813, 7 pages
doi:10.1155/2012/720813

Research Article

Monitoring Composites under Bending Tests with Infrared Thermography

Carosena Meola,[1] Giovanni Maria Carlomagno,[2] Carmela Bonavolontà,[3] and Massimo Valentino[3]

[1] *Department of Aerospace Engineering (DIAS), University of Naples Federico II, Via Claudio 21, 80125 Naples, Italy*
[2] *Department of Aerospace Engineering (DIAS), University of Naples Federico II, Piazzale Tecchio 80, 80125 Naples, Italy*
[3] *CNR-SPIN, Piazzale Tecchio 80, 80125 Naples, Italy*

Correspondence should be addressed to Carosena Meola, carmeola@unina.it

Received 2 August 2012; Accepted 2 October 2012

Academic Editor: Antoni Rogalski

The attention of the present paper is focused on the use of an infrared imaging device to monitor the thermal response of composite materials under cyclic bending. Three types of composites are considered including an epoxy matrix reinforced with either carbon fibres (CFRP) or glass fibres (GFRP) and a hybrid composite involving glass fibres and aluminium layers (FRML). The specimen surface, under bending, displays temperature variations pursuing the load variations with cooling down under tension and warming up under compression; such temperature variations are in agreement with the bending moment. It has been observed that the amplitude of temperature variations over the specimen surface depends on the material characteristics. In particular, the presence of a defect inside the material affects the temperature distribution with deviation from the usual bending moment trend.

1. Introduction

Infrared thermography (IRT) has proved helpfulness in many industrial and research fields as stated by the proceedings of the four main international symposia [1–4]. Amongst its many applications, an infrared imaging device is helpful for thermoelastic stress analysis (TSA) purposes [5, 6] and to monitor the surface temperature change (thermoelastic effect) which is experienced by a body when subjected to stress variations under load [7].

The thermoelastic effect was first conceived by Lord Kelvin (Thomson) in 1978 [8]. Many years later, in 1956 [9], Biot performed a thermodynamic analysis and formulated the classical thermoelastic equation, which expresses the change in temperature (T) of a solid in terms of the change in the sum of the principal stresses (σ). The temperature variation, under reversible and adiabatic conditions (i.e., in the elastic regime and neglecting heat transfer within the body and to the environment), for isotropic materials can be written as

$$\Delta T = -K T_a \, \Delta\sigma, \tag{1}$$

where T_a is the absolute body temperature, $\Delta\sigma$ is the mean stress amplitude, and K is the material thermoelastic constant. Equation (1) relates the temperature local variations to the stress variations. In particular, under adiabatic conditions, positive dilatation (tension) entails cooling of the material and vice versa. In metals, the thermoelastic limit is generally assumed [10] as an indication for the yielding point. In orthotropic materials as fibre-reinforced polymers (FRP) (1) is modified as

$$\Delta T = -\frac{T_a}{\rho c_p}(\alpha_1 \Delta\sigma_1 + \alpha_2 \Delta\sigma_2) \tag{2}$$

with α_1 and α_2 being the thermal expansion coefficients along the principal material directions and ρc_p the mean

volumetric heat capacity. For complex composite materials a direct relationship between the mean stress and TSA data is not possible [5]; however, in any case, the availability of the temperature map is important for materials characterization [11–16]. Thus, IRT represents a valuable mean for rapid determination of the fatigue limit (Risitano method) [11] and for damage evolution assessment.

It is worth nothing that within the fatigue concept IRT has been till now mainly used for TSA purposes associated with cyclic tension-compression tests [5, 6, 11–15]. Owing to bending tests, Luong [13] reports on the use of infrared thermography for detecting the onset of intrinsic dissipation, or damage indicator, owing to the thermomechanical coupling. The adopted procedure was to acquire a thermal image after a fixed number of cycles. In all these cases the analysis was driven towards the thermoplastic phase in which the temperature variation is significant and then easy to be measured [17]. A more difficult point is to deal with measurements of temperature variations experienced by the material during the elastic phase, that is, thermoelastic effects. Recently, Meola and Carlomagno tackled with such difficult endeavour; in particular, by choosing an appropriate image sampling rate, they succeeded in appraising the material temperature variations, which are due to both thermoelastic and thermoplastic effects, under low-energy impact [7, 18]. In particular, Meola and Carlomagno [18] supplied, through measurements of temperature rising and warm area extension, information about initiation and propagation of the impact damage in glass/epoxy materials.

As a next step in the analysis of thermoelastic effects, the thermal behaviour of composite materials under cyclic bending is addressed in this paper. Under cyclic bending the material undertakes tension and/or compression with cooling/warming effects involved. The main question, which arises, regards the possibility to acquire information on the material characteristics by simply monitoring the thermoelastic effects. Another question is if, which, and how material properties interfere with thermoelastic effects. And then, the attention of this work is focused on the use of an infrared imaging device for monitoring the thermal response of different types of composites during cyclic bending tests.

2. Experimental Analysis

The investigation is carried out in laboratory considering several different specimens made of different composite materials [17]. Specimens are subjected to bending tests with two different configurations, which are later described, and are also nondestructively inspected with lock-in thermography.

3. Materials

Several specimens are fabricated of three different types of composites owing to the composition (i.e., fibre and matrix).

(i) GFRP includes E glass fibres embedded in a low viscosity epoxy matrix. More specifically, this type of specimen is obtained by hand layup of eight epoxy adhesive preimpregnated unidirectional glass fibres and allowed to cure at ambient temperature. The stacking sequence is $[0_2, 90_4]_s$ with an overall specimen thickness $s = 2.9$ mm. Specimens are 30 mm wide and 134 mm long.

(ii) Gl specimens came from a type of FRML including 3 Al with 2 GFRP layers in between them; the overall thickness is $s = 1.5$ mm. This material is fabricated following industrial standards with curing in autoclave. Specimens are 30 mm wide and 148 mm long. In particular, one specimen, called Gl1, presents the outside surface covered with an aeronautical coating. In another one, called Gl2, the external aluminium layer was removed (through milling) from the side viewed by the infrared camera. And thus, the surface viewed by the infrared camera is practically that of a GFRP with the difference that there is no epoxy resin finishing.

(iii) CFRP is based on an epoxy-matrix (HFM 934) reinforced with T400 carbon fibres content of 55% by volume, fabricated by hand layup and autoclave curing. The stacking sequence is $([(0/90), \pm 45]_s)$, with an overall specimen thickness $s = 2.0$ mm. Specimens are 20 mm wide and 196 mm long.

3.1. Setup for Bending Tests

3.1.1. Bending Tests Are Performed with Two Configurations

Conf I. The specimen is fixed at the extreme A and is in contact with a punch in point C as sketched in Figure 1. Bending arises under the action of the force F that is applied cyclically at the extreme B and is directed downside. The infrared camera is positioned to see the surface on the top.

Conf II. The specimen is fixed at the extreme A as in *Conf I* with the exception that the punch is removed and then the configuration is that of a cantilever beam. In this case, tests are performed with the force acting cyclically in the direction upside-rest, down-rest, and upside-downside (downside-upside). For each type of test both surfaces (top and bottom) are monitored with the infrared camera. In particular, the bottom surface is viewed with the aid of a mirror placed at 45° underneath the specimen.

For both configurations the load is applied manually with care paid to assure adiabatic conditions. The amplitude is set with the aid of fixed supports, while the bending frequency is calculated as number of cycles in a given time measured by a chronometer.

Two infrared cameras are used, which are the SC3000 and the SC6000 (Flir Systems) both equipped with a QWIP detector working in the 8-9 μm infrared band. The standard acquisition rate for the SC3000 is 60 Hz full frame 320×240 pixels, but it can reach up 900 Hz with a reduced field of view of 16 lines. Conversely, the SC6000 offers a better thermal sensitivity and spatial resolution with 640×512 pixels full frame and a windowing option linked to frequency frame rate and temperature range.

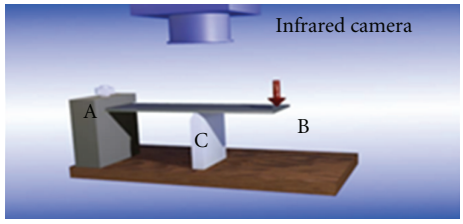

Figure 1: Sketch of the *Conf I* test setup.

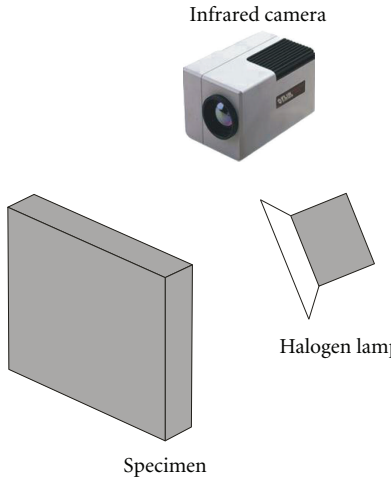

Figure 2: Setup for tests with lock-in thermography.

3.2. Setup for Nondestructive Inspection. Nondestructive tests are carried out with the SC3000 camera coupled with the Lock-in option and the IRLockIn software [19]. Thermal stimulation is performed with a halogen lamp; a sketch is shown in Figure 2; the heating frequency f is varied to inspect the material at different layers through the thickness according to the relationship:

$$\mu = \sqrt{\frac{\alpha}{\pi f}} \tag{3}$$

with μ the thermal diffusion length, α the thermal diffusivity, and f the heating frequency. Results are shown as phase images.

4. Bending Tests

Thermal images are taken in time sequence starting before loading application and ending after force removal to account for thermal phenomena with respect to the ambient temperature. The first image ($t = 0$) of the sequence (i.e., the ambient temperature of the specimen surface before load) is subtracted to each subsequent image so as to have a map of temperature difference ΔT:

$$\Delta T = T(i, j, t) - T(i, j, 0) \tag{4}$$

i and j representing lines and columns of the surface temperature map. Therefore, a sequence of ΔT images is created.

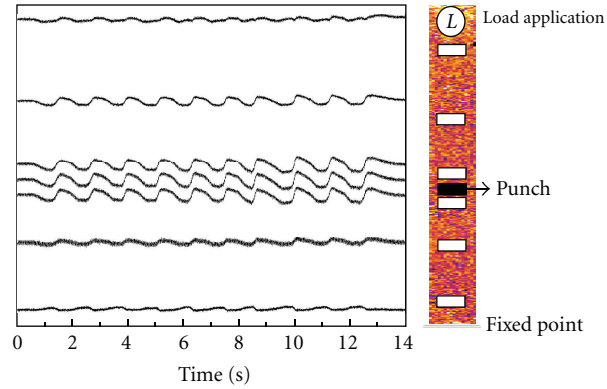

Figure 3: ΔT variation versus time in several areas located on the left and on the right of the punch under cyclic load for the Gl1 specimen.

4.1. Tests with Conf I. First, tests are carried out by monitoring, with the SC3000 camera, the top surface of the specimen while subjected to three points bending, which means employing the *Conf I* arrangement (Figure 1). In this case, thermal images are acquired in time sequence at 900 Hz; in general, each test involves ten cycles and so sequences of over 20 k images are obtained.

As an example, in Figure 3 are shown ΔT values against time at different positions over the Gl1 specimen under bending with *Conf I*. The specimen is undergoing a deflection of 10 mm at a frequency of about 0.85 Hz. In particular, each ΔT value is obtained by averaging the values inside a given area, which may be located on the left and on the right with respect to the punch position. More specifically, the position of each area (white rectangle) over the thermal image is shown on the right side in Figure 3; this image appears rotated by 90° counterclockwise with respect to the test setup (Figure 1). ΔT displays quasi-sinusoidal variations, which are perfectly coupled to the cyclic load.

Next, the temperature amplitude variation strongly depends on the position of the area over the specimen surface that is, on the area relative position with respect to its distance from the punch; this is in good agreement with the bending moment diagram. This feature is shown in Figure 4. In more details, in Figure 4(a) the ΔT variation moving left and right with respect to the punch position (*Conf I*) are reported. Such a distribution is similar for every specimen; of course, quantitative values depend on the specimen material (for this reason no scale is added). In Figure 4(b) the diagram of the bending moment is shown; this comes out from the theory of elasticity.

With reference to Figure 4(b), the maximum bending momentum $M_{b\max}$ is equal to the load (or force) F multiplied the distance b:

$$M_{b\max} = Fb \tag{5}$$

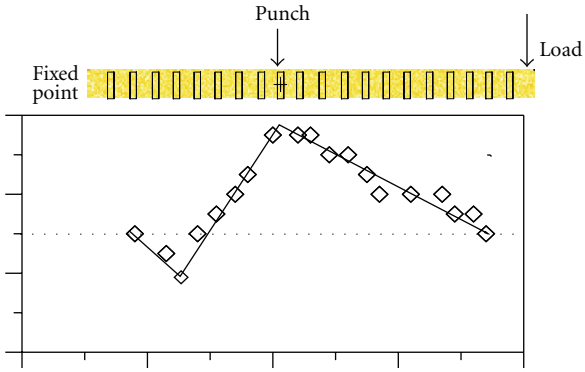

(a) Temperature amplitude distribution over the specimen surface under load

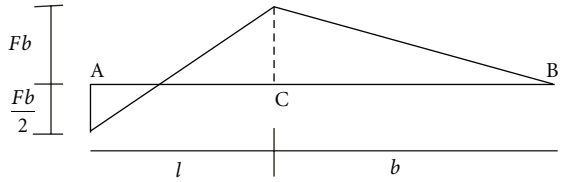

(b) Bending moment diagram

FIGURE 4: Comparison between temperature amplitude distribution (a) and bending moment diagram (b).

while the deflection of point B D_F is linked to the load F, the distances b and l, the area moment of inertia of the cross-section I, the specimen thickness s, the Young modulus E, and the stress σ through the following relationship:

$$D_F = \frac{Fb^2}{EI}\left(\frac{b}{3}+\frac{l}{4}\right) = \frac{2\sigma b}{Es}\left(\frac{b}{3}+\frac{l}{4}\right). \tag{6}$$

Considering (1) it is possible to write the relationship:

$$D_F Es = k\sigma = k'\Delta T \tag{7}$$

and then

$$\Delta T \propto D_F Es. \tag{8}$$

Of course, as already specified, (1) generally applies for isotropic materials, while, for composites, it takes a more complex form (2) involving components along fibres direction. However, stress analysis is outside the aim of the present paper, which is mainly focused on the possibility to assess the material integrity through the analysis of thermoelastics effects.

The average maximum ΔT values in the area over the punch (as indicated in Figure 4(a)) are compared in Figure 5 for the different types of specimens. As can be seen, the highest value is achieved for the Glare(R) specimen Gl1, while the value displayed by the Gl2 is slightly higher than the values obtained with both CFRP and GFRP. This because the ΔT amplitude depends on the material's thermal conductivity. Of course, the thermal conductivity of a composite material depends on both the matrix and the reinforce as well the stacking sequence. Within the present

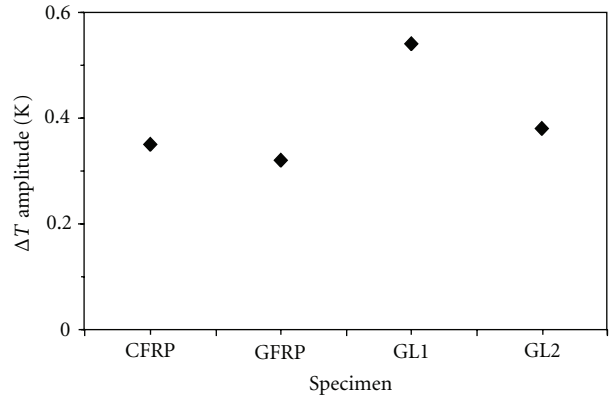

FIGURE 5: Maximum ΔT amplitude versus specimen type.

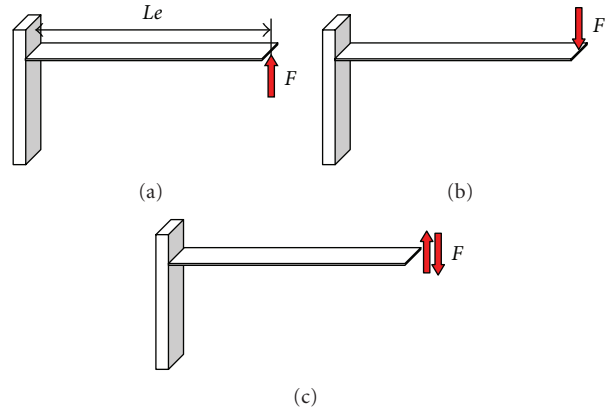

FIGURE 6: Sketch of the load application modes for tests with *Conf II*.

context, the main role is surely played by the outside layer, which is also affected by the presence of any coating. It has to be taken into account that the outside surface of any composite material is composed of a thin layer of epoxy resin, which, generally, acts as surface finishing, and that the thermal conductivity of the epoxy resin is lower than that of the carbon and the glass fibres. Thus, the distribution of ΔT values in Figure 5 is justified.

4.2. Tests with Conf II. These tests are performed by applying the load F in different ways as schematically depicted in Figure 6:

(i) from the bottom side directed upside (Figure 6(a)),

(ii) from the top side directed downside (Figure 6(b)),

(iii) for complete cycles upside-downside (Figure 6(c)) or downside-upside.

For each of the different load application modes, both of the specimen surfaces (top and bottom) are monitored with the SC6000 by acquiring sequences of images at 85 Hz during load application. The sequences of images are then transformed into sequences of ΔT images according to (4).

For a general comparison between data obtained with the two test configurations, the thermal response of the

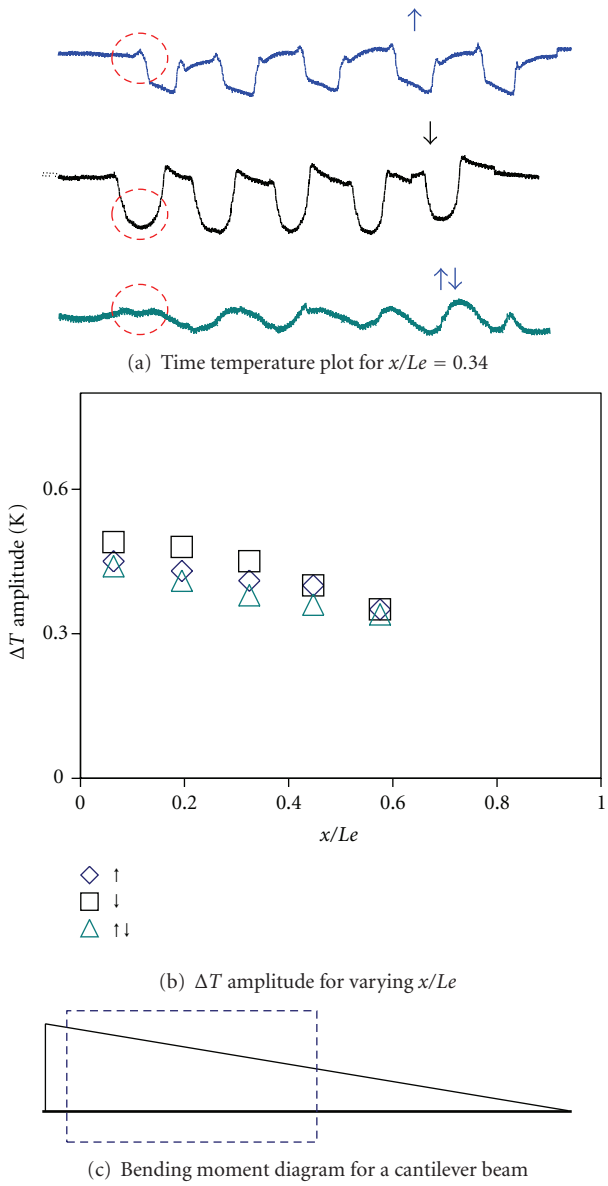

(a) Time temperature plot for $x/Le = 0.34$

(b) ΔT amplitude for varying x/Le

(c) Bending moment diagram for a cantilever beam

Figure 7: Behaviour of the Gl1 specimen by varying the load direction.

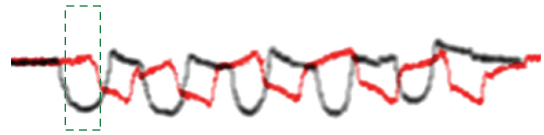

Figure 8: Variation of the temperature response for varying the load direction (red line upside as in Figure 6(a) and dark line downside as in Figure 6(b)).

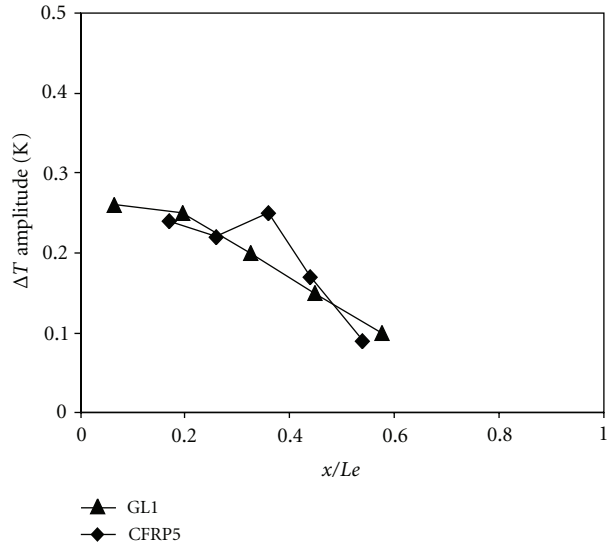

Figure 9: ΔT distribution on the bottom surface (under tension) of Gl1 and CFRP5 specimens with increasing x/Le.

Gl1 specimen is analyzed and compared with the bending moment in Figure 7. First, the ΔT value is extracted as average in a small area located at 34% from the fixture on the top surface and plotted for different load conditions in Figure 7(a); Le is the cantilever length (Figure 6(a)). Then, ΔT values obtained at different distances x along the length Le are plotted in Figure 7(b), while the bending moment is shown in Figure 7(c). For a direct comparison between the ΔT distribution and the bending moment, the area considered for thermal analysis is enveloped with the dashed rectangle.

Looking at Figure 7 two main considerations arise

(1) As already observed for data obtained with *Conf I* (Figure 4), the distribution of the ΔT amplitude is again in good agreement with the bending moment diagram.

(2) The temperature variation is in perfect concurrence with the load direction. In fact, following the red circle, the temperature increases, or decreases, depending on the surface being, respectively, under compression or under tension.

The latter aspect is better depicted in Figure 8 in which two ΔT profiles taken in the same area (same x/Le ratio), which is one time in compression (red line) and the other one in tension (dark line), are compared. More specifically, it is possible to see (by looking inside the dashed rectangle) the prompt inversion (rise/decrease) in the temperature distribution by changing load direction. However, it is also possible to see the higher amplitude with also a more regular trend displayed during cooling down with respect to that occurring during the warming up phase.

To gain information about the material behaviour under bending, maximum ΔT values, which were taken on the surface, being in tension, of two specimens Gl1 and CFRP5, are plotted against the x/Le ratio in Figure 9.

As a general comment, for both specimens, ΔT decreases with increasing the distance from the fixture; this is in agreement with the bending moment (Figure 7(c)). However, what catches eyes is the peak at about 37% of Le for the CFRP5 specimen. This may appear strange at first sight, but

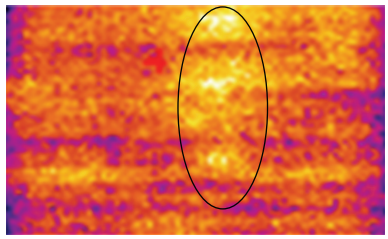

(a) $f = 0.5$ Hz

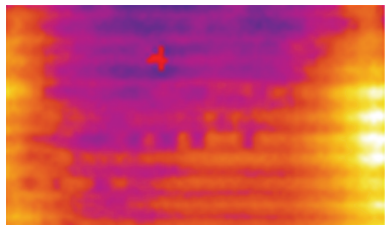

(b) $f = 0.15$ Hz

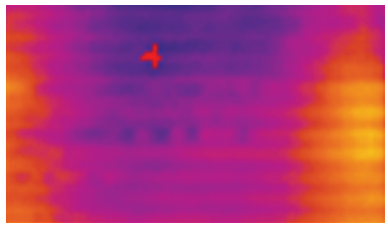

(c) $f = 0.09$ Hz

Figure 10: Phase images, taken at different heating frequency, for the specimen CFRP5.

it is easily explicable looking at the phase images, shown in Figure 10, which were obtained through nondestructive inspection with lock-in thermography (Figure 2). In fact, it is clear that the peak is caused by the anomaly (encircled in Figure 10(a)), which is present at low depth the viewed from one side of the specimen. Such anomaly tends to disappear going more in depth by decreasing the heating frequency f to 0.15 Hz (Figure 10(b)) and to 0.09 Hz (Figure 10(c)). There are some variations of the phase angle on the right edge (Figures 10(b) and 10(c)), but they have no effects on the ΔT distribution in Figure 9 since they are located in the part in which the specimen is clamped during bending tests and so not enclosed in the ΔT distribution. It is worth noting that, in Figure 10, the specimen appears rotated by 180° with respect to the position it had during bending tests (Figures 6–9); practically, in Figure 10, x/Le increases moving from right to left.

To better investigate the influence the buried anomaly has on the specimen thermoelastic behaviour under bending load, the ΔT distributions on both top and bottom surfaces, being one under compression and the other one under tension, are compared in Figure 11. It is possible to see that the anomaly, which is present on the bottom side, affects the temperature amplitude distribution. In fact, on the top side, the ΔT distribution attains higher values towards the fixture decreasing with increasing Le in good compliance with the bending moment (Figure 7(c)). Instead the ΔT

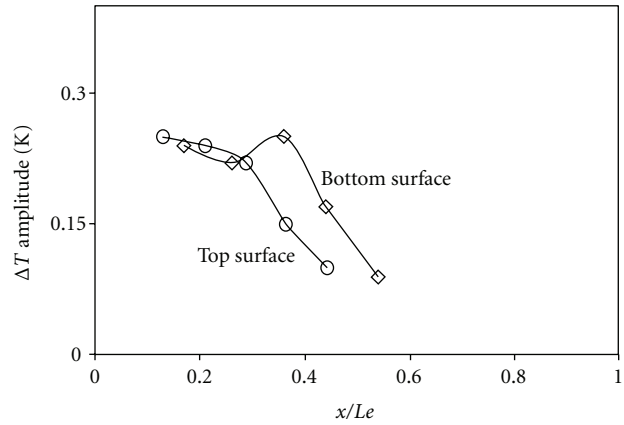

Figure 11: Comparison between ΔT distribution on top (under compression) and bottom (under tension) surfaces of the specimen CFRP5.

amplitude distribution on the bottom side presents the already mentioned peak at 37% of Le which corresponds to the position of the anomaly (Figure 10(a)). This means that the presence of a defect does not allow the material to freely expand/contract under tension/compression, but increases the local material resistance to the deformation. This feature manifests itself through a subsequent local thermal signature. Therefore, monitoring the thermal response of the material to a bending force may supply two types of information:

(i) material mechanical characterization through the link between the temperature variation and the stress amplitude (1) or (2),

(ii) detection of buried defects.

5. Conclusions

The thermal response to cyclic bending of different types of specimens was analyzed with infrared thermography. Two different bending configurations were considered, with the specimen either hanged as a cantilever beam, or with a punch as central support. For both configurations, the load was manually applied with care paid to assure adiabatic conditions. As a main finding, for all test conditions and for all the specimens, the temperature variations follow the bending moment trend. Deviation from such a trend was observed which, in our opinion, is due to the presence of anomalies in the specimen material. This was ascertained through nondestructive evaluation of specimens with lock-in thermography.

The added value of this work resides in the possibility to gain, in a fast and easy way, through the use of a simple hand-handled mechanism and an infrared imaging device, information on the material thermal characteristics. This feature may be very important for the nondestructive evaluation of composite materials considering the even broad production of such materials and the need for their fast and reliable characterization.

It has to be, however, pointed out that the present study is only a preliminary research and new tests are under way, which include a wider variety of specimens and power-driven load application with change of parameters such as bending amplitude and frequency.

References

[1] Proceedings of the Annual SPIE Thermosense Conferences, Bellingham, Wash, USA, 1978.

[2] Proceedings of the Advanced Infrared Technology & Applications (AITA), 1991.

[3] Proceedings of the Biennial Quantitative Infrared Thermography (QIRT) Conferences, 1992.

[4] Proceedings of the InfraMation, 2000.

[5] J. M. Dulieu-Barton, T. R. Emery, S. Quinn, and P. R. Cunningham, "A temperature correction methodology for quantitative thermoelastic stress analysis and damage assessment," *Measurement Science and Technology*, vol. 17, no. 6, pp. 1627–1637, 2006.

[6] U. Galietti, D. Modugno, and L. Spagnolo, "A novel signal processing method for TSA applications," *Measurement Science and Technology*, vol. 16, no. 11, pp. 2251–2260, 2005.

[7] C. Meola and G. M. Carlomagno, "Infrared thermography of impact-driven thermal effects," *Applied Physics A*, vol. 96, no. 3, pp. 759–762, 2009.

[8] W. Thomson, "On the thermoelastic, thermomagnetic and pyroelectric properties of matters," *Philosophical Magazine*, vol. 5, pp. 4–27, 1978.

[9] M. A. Biot, "Thermoelasticity and irreversible thermodynamics," *Journal of Applied Physics*, vol. 27, no. 3, pp. 240–253, 1956.

[10] M. G. Beghi, C. E. Bottani, and G. Caglioti, "Irreversible thermodynamics of metals under stress," *Res Mechanica*, vol. 19, no. 4, pp. 365–379, 1986.

[11] G. La Rosa and A. Risitano, "Thermographic methodology for rapid determination of the fatigue limit of materials and mechanical components," *International Journal of Fatigue*, vol. 22, no. 1, pp. 65–73, 2000.

[12] G. Fargione, A. Geraci, G. La Rosa, and A. Risitano, "Rapid determination of the fatigue curve by the thermographic method," *International Journal of Fatigue*, vol. 24, no. 1, pp. 11–19, 2002.

[13] M. P. Luong, "Fatigue limit evaluation of metals using an infrared thermographic technique," *Mechanics of Materials*, vol. 28, no. 1–4, pp. 155–163, 1998.

[14] P. R. Cunningham, "Thermoelastic characterisation of damage around a circular hole in a GRP component," *Key Engineering Materials*, vol. 204-205, pp. 453–463, 2001.

[15] R. J. H. Paynter and A. G. Dutton, "The use of a second harmonic correlation to detect damage in composite structures using thermoelastic stress measurements," *Strain*, vol. 39, no. 2, pp. 73–78, 2003.

[16] Ö. S. Şahin, M. Selek, and Ş. Kahramanlı, "Investigation of bending fatigue of composite plates by using infrared thermography," *Advanced Materials Research*, vol. 268–270, pp. 406–411, 2011.

[17] C. Bonavolontà, M. Valentino, C. Meola, and G. M. Carlomagno, "NDT of polymer nanocomposite for structural applications using electromagnetic techniques," *International Journal of Applied Electromagnetics and Mechanics*, vol. 39, no. 1–4, pp. 363–368, 2012.

[18] C. Meola and G. M. Carlomagno, "Impact damage in GFRP: new insights with infrared thermography," *Composites A*, vol. 41, no. 12, pp. 1839–1847, 2010.

[19] C. Meola and G. M. Carlomagno, "Infrared thermography in non-destructive inspection: theory and practice," in *Recent Advances in Non Destructive Inspection*, C. Meola, Ed., pp. 89–123, Nova Science, New York, NY, USA, 2010.